The Planetary Science Journal, 3:90 (10pp), 2022 April https://doi.org/10.3847/PSJ/ac6342

Asteroid Polarimetric Phase Behavior in the Near-infrared: S- and C-complex Objects

Joseph R. Masiero[1], S. Tinyanont[2], and Maxwell A. Millar-Blanchaer[3]
[1] Caltech/IPAC, 1200 E. California Boulevard, MC 100-22, Pasadena, CA 91125, USA; jmasiero@ipac.caltech.edu
[2] University of California, Santa Cruz, CA 95064, USA
[3] Department of Physics, University of California, Santa Barbara, CA 93106, USA
Received 2022 February 11; revised 2022 March 28; accepted 2022 March 29; published 2022 April 22

Abstract

We present the first results of our survey of asteroid polarization phase curves in the near-infrared *J* and *H* bands using the WIRC+Pol instrument on the Palomar 200-inch telescope. We confirm through observations of standard stars that WIRC+Pol can reach the 0.1% precision needed for asteroid phase curve characterization, and we show that C-complex asteroids could act as an alternate calibration source, as they show less wavelength variation than stellar polarized standards. Initial polarization phase curve results for S-complex asteroids show a shift in behavior as a function of wavelength from visible to near-infrared bands, extending previously observed trends. Full near-infrared polarization phase curve characterization of individual asteroids will provide a unique constraint on surface composition of these objects by probing the wavelength dependence of albedo and index of refraction of the surface material.

Unified Astronomy Thesaurus concepts: Asteroids (72); Asteroid surfaces (2209); Polarimetry (1278)

1. Introduction

Light scattered by asteroids encodes information about the physical makeup of the surface material. The way that light is polarized as it is scattered, as well as the dependence of that polarization on the phase angle of the observations (the Sun–asteroid–observer angle, α), provides unique constraints on the surface properties. Incoming light from the Sun incident on the asteroid's surface will be initially unpolarized. Simple scattering models predict that the scattered light will be polarized perpendicular to the scattering plane, with a maximum near $\alpha \sim 90°$. However, observations of atmosphereless bodies, initially the Moon and then later asteroids, showed that at phase angles $\alpha < 20°$ the observed polarization direction is reversed and instead shows polarization parallel to the scattering plane (Lyot 1929; Hopfield 1966; Zellner et al. 1974). Detailed scattering models have shown that this reversal of polarization at small phase angles is due to the coherent backscatter mechanism that also drives the photometric opposition effect, where multiply scattered electromagnetic waves interfere constructively and destructively in different proportions as a function of phase (Shkuratov et al. 1994; Muinonen et al. 2002, 2009).

The relationship between the polarization of the scattered light and phase angle can be described by key quantities that trace physical surface properties. For studies of asteroids the angle of polarization θ_r is typically measured with respect to the scattering plane and the polarization P_r is given in this rotated frame. Positive P_r values are assigned to polarization perpendicular to the plane ($\theta_r = 0°$), and negative values are assigned to polarization in the plane ($\theta_r = 90°$). The curve traced by P_r as a function of phase angle α can be described by four key metrics: (1) the inversion angle α_0, which is the phase angle at which the polarization transitions from positive to negative; (2) the slope h of the curve at the inversion angle; (3) the minimum polarization $P_{\rm min}$ reached in the negative branch; and (4) the phase angle $\alpha_{\rm min}$ at which $P_{\rm min}$ is reached. Geometric albedo of the surface has been shown to be correlated with h and $P_{\rm min}$ (Cellino et al. 2015), while the inversion angle is related to the index of refraction of the surface material (Masiero et al. 2009; Gil-Hutton & García-Migani 2017).

These relationships result in the polarization phase behavior showing a dependence on the composition of an asteroid's surface, as traced by its spectral taxonomic classification. A major survey of visible-light asteroid polarization was carried out using the Complejo Astronómico El Leoncito (CASLEO) facility in Argentina (Gil-Hutton & Cañada-Assandri 2011; Cañada-Assandri et al. 2012; Gil-Hutton & Cañada-Assandri 2012), covering a wide range of taxonomic classes. The CASLEO results showed that within a taxonomic class objects tend to show consistent polarimetric behavior, while between classes changes in h, $P_{\rm min}$, $\alpha_{\rm min}$, and α_0 are observed and tend to follow compositional trends. This survey has continued in recent years with the aim of probing smaller objects to search for size-dependent behaviors, correlations with asteroid family, and end-member taxonomies.

Asteroid polarization should also depend on the wavelength of light used for the observations, as both reflectivity and index of refraction can have wavelength dependencies. While some asteroids, such as the B and C types, have roughly flat spectra from the visible to the near-infrared, the S-complex objects show a red spectral slope, and this reflectivity change would be predicted to correspond to a change in h slope and $P_{\rm min}$. Belskaya et al. (2009) obtained asteroid polarimetric phase curves spanning the *UBVRI* bandpasses for a range of asteroid compositions. They found a wavelength dependence of a few tenths of a percent polarization per micron across most phase angles, with S types at larger phases showing the largest change. However, contrary to expectations, the sign of the change did not reverse at the inversion angle, indicating that, instead of a pivot around inversion angle, the curves were offset. In a different survey, Pan & Ip (2022) used the TriPol instrument to observe polarimetric phase curves in the g', r',

and i' bands, but they found only minimal changes with wavelength.

Up until now, asteroid polarization surveys have focused on wavelengths shortward of $\sim$1 μm. The first asteroid surveys were conducted primarily in the *B* and *G* bands, as they made use of photomultiplier tubes that were preferentially sensitive to those wavelengths (e.g., Zellner & Gradie 1976). Later surveys such as those using the CASLEO instrument (e.g., Cellino et al. 2005) spanned the *U, B, V, R,*and*I* bands, though the majority of observations were obtained in *V* and *R*, where an asteroid's reflected light flux peaks. Here we report our first results from a survey of asteroid polarization phase curves in the near-infrared *J* (1.25 μm) and *H* (1.64 μm) bands. This is the first such survey of asteroid polarization at these wavelengths. It should be noted that there have been previous investigations of comet polarizations at these wavelengths (e.g., Oishi et al. 1978; Jones et al. 2008; Kwon et al. 2019); however, they generally have been at much higher phase angles, where polarizations are larger, or have not had sufficient instrumental accuracy to characterize the negative polarization branch. In this paper we describe our observing methodology and present early results from our observations. Future work will focus on constraining the polarization phase behavior of specific objects, as well as compositional groupings and subclasses (e.g., the Barbarian asteroids).

2. Observations

To carry out our survey, we make use of the newly commissioned polarimetric mode for the Wide-field Infrared Camera (WIRC) instrument on the 200-inch Palomar telescope. WIRC is a near-infrared optimized camera mounted at the telescope's prime focus, providing an $8\farcm7$-wide field of view with $0\farcs25$ pixels (Wilson et al. 2003). The 200-inch Palomar telescope is equatorially mounted, meaning that WIRC will maintain an unchanging orientation with respect to the sky and that there are no fold mirrors in the light path, making it an ideal choice for adding polarimetric sensitivity.

A polarimetric enhancement to WIRC, called WIRC+Pol, was deployed in 2017 (Tinyanont et al. 2019b) using a novel combination of a quarter-wave plate in series with polarization grating (PG) to simultaneously measure the four different components of linear polarization (0°, 45°, 90°, 135°; referred to as $+Q$, $+U$, $-Q$, and $-U$ in the Stokes vector formalism). The PG element splits the light into the four polarization components while simultaneously dispersing each into low-resolution ($R \sim 100$) spectra, providing spectropolarimetric sensitivity as well. Because of this four-way dispersion, the field of view is restricted by an upstream mask, and observations of extended objects are more complicated to untangle. Additionally, only the *J* and *H* bands are usable in this spectropolarimetric mode, as much of the field for *K*-band observations would be dispersed beyond the detector.

In 2019, WIRC+Pol was upgraded with a half-wave plate (HWP) upstream of the PG (Tinyanont et al. 2019a). By rotating the HWP through four different orientations ($\theta_{\rm HWP} = 0°$, $22\fdg5$, 45°, $67\fdg5$), the polarization of the incoming light becomes rotated by $2\theta_{\rm HWP}$, effectively swapping the Stokes parameter that contributes to each of the four beams leaving the PG. This beam swapping allows for slight differences in the optical paths between the beams to be corrected for and pushes the polarimetric precision of WIRC +Pol to <0.1% when sufficient signal-to-noise ratio is obtained.

Our typical observing sequence for the data presented here consisted of a series of four cycles through the four HWP angles, for a total of 16 exposures before switching to the other filter. For observations in 2021, we enhanced this cadence by observing A–B pairs to better constrain the background for faint targets. All targets observed in 2019 were brighter than $J < 10.5$ mag and so did not show any systematic differences due to lack of A–B pairs. In this mode, we obtained four HWP cycles in *J* band at position A, four cycles in *H* band at position A, four cycles in *H* at position *B*, and finally four cycles in *J* at position B. This 64-image set was our primary observing unit and causes the UT midpoint of both bands to be the same. With readout, filter change, and dithering overheads, this observing block takes approximately 20 minutes of wall-clock time for bright sources ($J = 6$–11 mag, exposure times of 1–5 s) and about 50 minutes for faint sources ($J = 11$–13 mag, exposure time of 30 s). For our faintest targets this sequence was repeated as necessary to obtain sufficient flux for high-precision polarimetry.

3. Data Reduction and Calibration Verification

All image calibration and polarization measurements were accomplished using the WIRC+Pol Data Reduction Pipeline available publicly on GitHub.[4] This pipeline makes use of the `Numpy`, `Scipy`, `Astropy`, `PhotUtils`, and `Matplotlib` Python packages. The pipeline extracts polarimetric measurements from each of the four diffracted beams and combines them over the HWP rotations to determine the final polarization degree and angle. The WIRC+Pol Data Reduction Pipeline is described in Tinyanont et al. (2019b), and updated details are available at the documentation website.[5]

In order to calibrate the raw FITS images from WIRC+Pol, we dark-subtract and flatten each individual image before extracting the polarimetric measurements. A master dark file was created each night for each exposure time, composed of 30 dark frames from the beginning of the night and 30 from the end. Dome flats were obtained each night for both bands, and a master flat field was created with all the optical elements in the beam.

For data from our 2019 runs, background levels were interpolated from nearby regions on the detector. The observations from 2021 were taken in an A–B observing sequence, and so background levels from the B frames were subtracted from the same pixels as the location of the data in the A frames, and vice versa. As described in Tinyanont et al. (2019a), to correct for beam throughput, the differences for *Q* and *U* beam pairs from each wave plate position were calculated and then averaged over all wave plate orientations. Because WIRC+Pol disperses the light in each band, final *Q* and *U* values are output as a function of wavelength. For this work, we provide the error-weighted mean of the polarization degree *P* and polarization angle θ for wavelengths with sufficient throughput. This allows us to improve our signal-to-noise ratio while investigating polarization changes from visible to *J* to *H* bands. Future work will explore the polarization as a function of wavelength within each band.

[4] https://github.com/WIRC-Pol/wirc_drp
[5] https://wircpol.readthedocs.io/

Table 1
WIRC+Pol Standard Star Results

Target	Date	Midpoint UT	Filter	Literature Polarization Value	Literature Polarization Angle (deg E of N)	Measured Polarization	Measured Angle (deg)
Polarized Standards							
HD 17747			*V*	0.89 ± 0.06%	139.7 ± 1.8		
HD 17747	2021-09-04	10:27	*J*	0.41 ± 0.06%	139.7 ± 1.8	0.354 ± 0.025%	125.8 ± 3.7
HD 17747	2021-09-04	10:27	*H*	0.22 ± 0.06%	139.7 ± 1.8	0.234 ± 0.009%	116.1 ± 2.0
HD 17747	2021-11-08	07:57	*J*	0.41 ± 0.06%	139.7 ± 1.8	0.336 ± 0.011%	124.7 ± 2.2
HD 17747	2021-11-08	07:57	*H*	0.22 ± 0.06%	139.7 ± 1.8	0.214 ± 0.011%	109.5 ± 1.6
HD 30870			*V*	1.34 ± 0.2%	66.0 ± 4.3		
HD 30870	2019-08-30	11:31	*J*	0.62 ± 0.2%	66.0 ± 4.3	0.643 ± 0.070%	86.8 ± 2.3
HD 35395			*V*	1.52 ± 0.20%	147 ± 3.8		
HD 35395	2021-02-03	03:51	*J*	0.70 ± 0.20%	147 ± 3.8	0.572 ± 0.010%	140.6 ± 1.0
HD 35395	2021-02-03	03:51	*H*	0.38 ± 0.20%	147 ± 3.8	0.293 ± 0.002%	138.2 ± 1.0
HD 46660			*V*	1.75 ± 0.20%	13 ± 3		
HD 46660	2021-02-03	05:13	*J*	0.81 ± 0.20%	13 ± 3	0.983 ± 0.012%	9.3 ± 0.2
HD 46660	2021-02-03	05:13	*H*	0.44 ± 0.20%	13 ± 3	0.713 ± 0.011%	12.6 ± 0.2
HD 50064			*V*	2.21 ± 0.18%	150 ± 2.3		
HD 50064	2019-03-17	03:47	*J*	1.02 ± 0.18%	150 ± 2.3	1.182 ± 0.010%	144.9 ± 0.5
HD 50064	2019-03-17	04:10	*H*	0.55 ± 0.18%	150 ± 2.3	0.885 ± 0.005%	145.8 ± 0.9
HD 50064	2019-03-17	05:54	*J*	1.02 ± 0.18%	150 ± 2.3	1.185 ± 0.015%	144.8 ± 0.7
HD 50064	2019-03-17	06:04	*H*	0.55 ± 0.18%	150 ± 2.3	0.716 ± 0.013%	149.4 ± 1.0
HD 58624			*V*	1.11 ± 0.07%	27 ± 1.8		
HD 58624	2019-03-17	06:42	*J*	0.51 ± 0.07%	27 ± 1.8	0.341 ± 0.014%	26.4 ± 1.5
HD 58624	2019-03-17	06:23	*H*	0.28 ± 0.07%	27 ± 1.8	0.302 ± 0.016%	18.9 ± 1.3
HD 58624	2021-02-03	06:48	*J*	0.51 ± 0.07%	27 ± 2	0.365 ± 0.017%	22.9 ± 1.4
HD 58624	2021-02-03	06:48	*H*	0.28 ± 0.07%	27 ± 2	0.230 ± 0.006%	21.4 ± 1.0
HD 58624	2021-11-08	12:53	*J*	0.56 ± 0.07%	26.9 ± 1.8	0.734 ± 0.052%	12.6 ± 1.2
HD 58624	2021-11-08	12:53	*H*	0.28 ± 0.07%	26.9 ± 1.8	0.421 ± 0.009%	19.5 ± 1.7
HD 144639			*V*	1.06 ± 0.05%	87 ± 1.3		
HD 144639	2021-06-26	06:55	*J*	0.49 ± 0.05%	87 ± 1.3	0.593 ± 0.023%	77.2 ± 0.7
HD 144639	2021-06-26	06:55	*H*	0.26 ± 0.05%	87 ± 1.3	0.315 ± 0.008%	90.3 ± 0.2
HD 152466			*V*	1.01 ± 0.00%	88.9 ± 0.4		
HD 152466	2019-03-17	11:42	*J*	0.47 ± 0.00%	88.9 ± 0.4	0.601 ± 0.014%	83.4 ± 0.3
HD 188618			*V*	2.40 ± 0.20%	179 ± 2.4		
HD 188618	2019-08-30	04:34	*J*	1.11 ± 0.20%	179 ± 2.4	1.206 ± 0.024%	166.9 ± 0.4
HD 188618	2019-08-30	06:30	*J*	1.11 ± 0.20%	179 ± 2.4	1.333 ± 0.037%	164.6 ± 0.6
HD 208205			*V*	0.70 ± 0.07%	145 ± 3		
HD 208205	2021-05-30	10:39	*J*	0.32 ± 0.07%	145 ± 3	0.401 ± 0.010%	135.2 ± 1.7
HD 208205	2021-05-30	10:39	*H*	0.18 ± 0.07%	145 ± 3	0.313 ± 0.004%	127.4 ± 2.5
HD 220859			*V*	0.58 ± 0.03%	125.8 ± 1.4		
HD 220859	2021-09-04	07:15	*J*	0.27 ± 0.03%	125.8 ± 1.4	0.262 ± 0.043%	81.2 ± 2.2
HD 220859	2021-09-04	07:15	*H*	0.15 ± 0.03%	125.8 ± 1.4	0.206 ± 0.030%	101.1 ± 1.7
HD 220859	2021-11-08	04:04	*J*	0.27 ± 0.03%	125.8 ± 1.4	0.236 ± 0.035%	118.4 ± 5.7
HD 231195			*V*	3.67 ± 0.06%	34.4 ± 0.5		
HD 231195	2021-06-26	10:26	*J*	1.69 ± 0.06%	34.4 ± 0.5	1.250 ± 0.121%	44.9 ± 5.2
Unpolarized Standards							
HD 26515			*V*	0.02 ± 0.05%			
HD 26515	2019-08-30	08:54	*J*	0.02 ± 0.05%		0.141 ± 0.017%	68.5 ± 4.0
HD 26515	2019-08-30	11:50	*J*	0.02 ± 0.05%		0.198 ± 0.030%	103.3 ± 2.8
HD 35076			*V*	0.07 ± 0.03%			
HD 35076	2021-09-04	12:22	*J*	0.07 ± 0.03%		0.125 ± 0.022%	41.9 ± 8.6
HD 35076	2021-09-04	12:22	*H*	0.07 ± 0.03%		0.208 ± 0.018%	77.3 ± 2.1
HD 35076	2021-11-08	11:10	*J*	0.07 ± 0.03%		0.318 ± 0.060%	89.9 ± 2.1
HD 35076	2021-11-08	11:10	*H*	0.07 ± 0.03%		0.257 ± 0.006%	71.2 ± 1.4
HD 40724			*V*	0.05 ± 0.03%			
HD 40724	2021-02-03	04:13	*J*	0.05 ± 0.03%		0.094 ± 0.026%	49.2 ± 3.0
HD 40724	2021-02-03	04:13	*H*	0.05 ± 0.03%		0.217 ± 0.007%	121.6 ± 0.1
HD 51596			*V*	0.02 ± 0.03%			
HD 51596	2019-03-17	04:35	*J*	0.02 ± 0.03%		0.074 ± 0.013%	46.3 ± 5.0
HD 51596	2019-03-17	04:28	*H*	0.02 ± 0.03%		0.185 ± 0.008%	114.4 ± 2.9

Table 1
(Continued)

Target	Date	Midpoint UT	Filter	Literature Polarization Value	Literature Polarization Angle (deg E of N)	Measured Polarization	Measured Angle (deg)
HD 51596	2019-03-17	05:48	*J*	0.02 ± 0.03%		0.163 ± 0.013%	31.9 ± 3.7
HD 51596	2019-03-17	05:36	*H*	0.02 ± 0.03%		0.064 ± 0.006%	53.0 ± 0.5
HD 65970			*V*	0.04 ± 0.04%			
HD 65970	2019-03-17	07:05	*J*	0.04 ± 0.04%		0.032 ± 0.012%	48.1 ± 7.2
HD 65970	2019-03-17	07:28	*H*	0.04 ± 0.04%		0.058 ± 0.009%	90.4 ± 0.1
HD 71371			*V*	0.05 ± 0.05%			
HD 71371	2021-02-03	06:22	*J*	0.05 ± 0.05%		0.080 ± 0.007%	44.7 ± 3.8
HD 71371	2021-02-03	06:22	*H*	0.05 ± 0.05%		0.052 ± 0.007%	66.0 ± 2.1
HD 79096			*V*	0.03 ± 0.04%			
HD 79096	2021-02-03	07:11	*J*	0.03 ± 0.04%		0.031 ± 0.006%	110.1 ± 5.1
HD 79096	2021-02-03	07:11	*H*	0.03 ± 0.04%		0.080 ± 0.007%	43.0 ± 0.8
HD 79096	2021-05-30	03:49	*J*	0.03 ± 0.04%		0.169 ± 0.044%	71.4 ± 10.6
HD 79096	2021-05-30	03:49	*H*	0.03 ± 0.04%		0.186 ± 0.006%	90.3 ± 0.2
HD 105262			*V*	0.07 ± 0.04%			
HD 105262	2021-02-03	11:20	*J*	0.07 ± 0.04%		0.158 ± 0.037%	23.2 ± 2.9
HD 105262	2021-02-03	11:20	*H*	0.07 ± 0.04%		0.131 ± 0.005%	69.9 ± 2.9
HD 105928			*V*	0.037 ± 0.034%			
HD 105928	2021-06-26	03:55	*J*	0.037 ± 0.034%		0.061 ± 0.012%	85.7 ± 4.0
HD 105928	2021-06-26	03:55	*H*	0.037 ± 0.034%		0.152 ± 0.006%	0.9 ± 0.2
HD 136497			*V*	0.04 ± 0.01%			
HD 136497	2019-03-17	11:05	*J*	0.04 ± 0.01%		0.046 ± 0.010%	72.6 ± 5.4
HD 136497	2019-03-17	10:43	*H*	0.04 ± 0.01%		0.122 ± 0.005%	69.9 ± 4.7
HD 196348			*V*	0.06 ± 0.04%			
HD 196348	2019-08-30	04:49	*J*	0.06 ± 0.04%		0.476 ± 0.096%	52.9 ± 12.9
HD 196348	2019-08-30	06:15	*J*	0.06 ± 0.04%		0.458 ± 0.121%	149.9 ± 5.2
HD 197577			*V*	0.07 ± 0.04%			
HD 197577	2021-06-26	07:44	*J*	0.07 ± 0.04%		0.123 ± 0.021%	88.9 ± 2.5
HD 197577	2021-06-26	07:44	*H*	0.07 ± 0.04%		0.058 ± 0.005%	125.9 ± 1.5
HD 197577	2021-09-04	05:46	*J*	0.07 ± 0.04%		0.157 ± 0.028%	88.9 ± 2.4
HD 197577	2021-09-04	05:46	*H*	0.07 ± 0.04%		0.076 ± 0.007%	90.0 ± 0.1
HD 197577	2021-11-08	02:07	*J*	0.07 ± 0.04%		0.311 ± 0.029%	151.0 ± 3.6
HD 197577	2021-11-08	02:07	*H*	0.07 ± 0.04%		0.156 ± 0.018%	41.3 ± 2.0
HD 203843			*V*	0.06 ± 0.04%			
HD 203843	2019-08-30	06:59	*J*	0.06 ± 0.04%		0.285 ± 0.053%	21.9 ± 4.1
HD 203843	2019-08-30	08:36	*J*	0.06 ± 0.04%		0.252 ± 0.069%	68.8 ± 3.2
HD 203843	2021-05-30	10:18	*J*	0.06 ± 0.04%		0.219 ± 0.033%	118.6 ± 1.8
HD 203843	2021-05-30	10:18	*H*	0.06 ± 0.04%		0.322 ± 0.033%	113.4 ± 0.4
HD 221356			*V*	0.02 ± 0.01%			
HD 221356	2021-09-04	07:50	*J*	0.02 ± 0.01%		0.094 ± 0.060%	64.7 ± 12.0
HD 221356	2021-09-04	07:50	*H*	0.02 ± 0.01%		0.083 ± 0.014%	53.6 ± 6.5

Table 1 presents our measurements of the polarized and unpolarized stars observed as part of our survey. The spectro-polarimetric measurements from WIRC+Pol were combined, weighting by their uncertainties, to generate the broadband polarization and angles given here. Literature polarization values for each object at *V* band are given, as well as the estimated polarization for these standards at *J* and *H* wavelengths based on literature measurements (see discussion below). Angles of polarization are given in degrees east of north.

In order to validate the calibration of the instrument and data reduction software and ensure that there were no unexpected night-to-night variations, we obtained measurements of polarized and unpolarized standard stars on each observing night. Standards were chosen to be as close as possible on-sky to our asteroid targets and were observed such that their hour angle was similar to that of our asteroid targets. For our observing dates in 2019 we repeated standards before and after the targets to constrain any short-term variations, but our results were repeatable within the expected error ($\Delta P \sim 0.1\%$), and so for future observing runs standards were only observed once per night to increase the time available for asteroid observations.

Polarized and unpolarized standards were chosen from the Heiles (2000) compilation of standard stars for polarimetry. The compiled literature measurements were from a variety of source works, but all were obtained at visible wavelengths. Polarization of stellar light by interstellar dust, which is the main source of polarization in bright stars, shows a distinct dependence on wavelength (Serkowski et al. 1975). To estimate the expected polarization level of our polarized standards at the *J* and *H* bands, we use Equation (4) from Serkowski et al. (1975):

$$P/P_{\max} = \exp[-1.15 \ln^2(\lambda_{\max}/\lambda)],$$

where P is the expected polarization, $P_{\max}$ is the maximum polarization (assumed to be the literature value), $\lambda_{\max}$ is the wavelength of maximum polarization (assumed to be 0.55 μm),

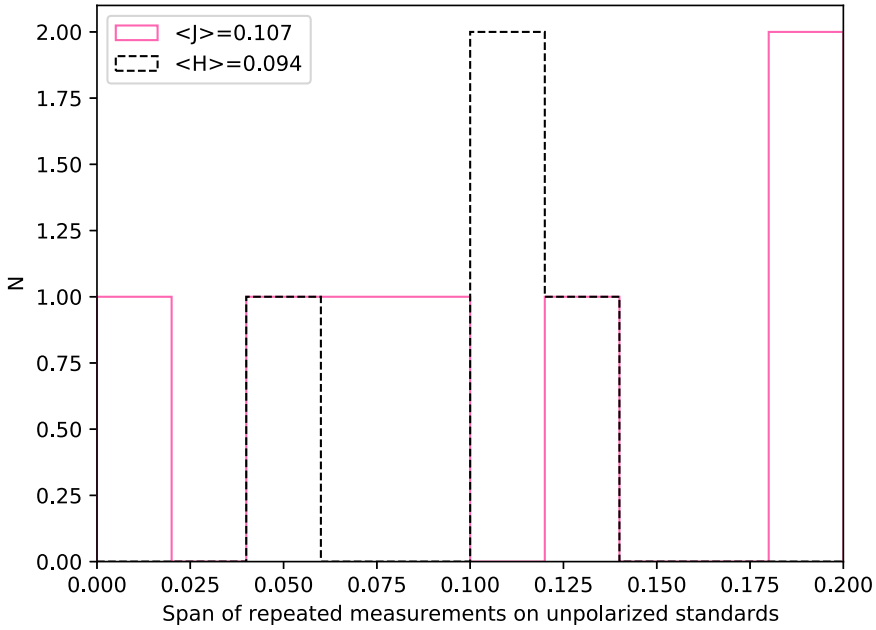

Figure 1. Histogram showing the changes in measured polarization between observations for nominally unpolarized standard stars. *X*-axis units are in percent polarization, and the mean for each band, given in the legend, is consistent with 0.1% overall system precision.

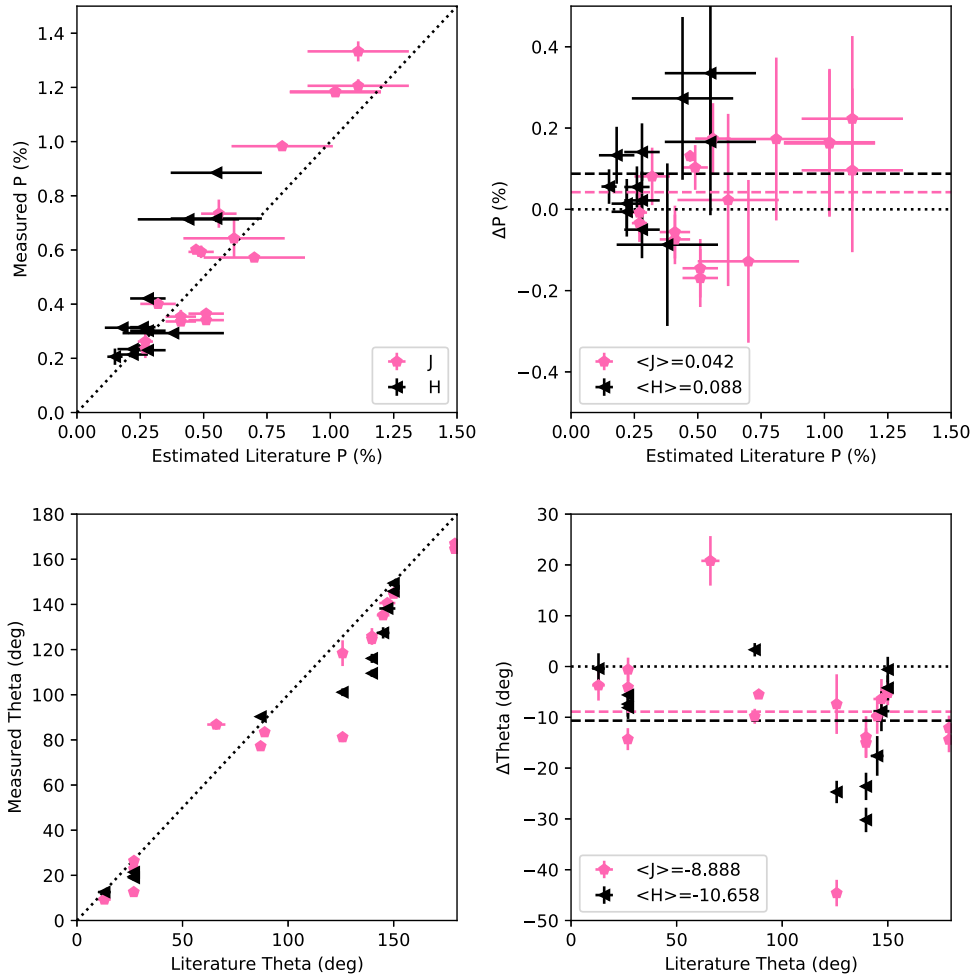

Figure 2. Comparison of predicted and measured polarization degrees and angles for polarized standard stars. The top left panel shows the measured polarization value against the literature values corrected for wavelength changes. The top right panel shows the difference in polarization (measured–literature) against the scaled literature values. The bottom left panel shows the measured angle of polarization compared to the literature angle, and the bottom right panel shows the difference in angle compared to the literature angle. Both difference plots include dashed lines showing the mean offset values, with the value for each band given in the legend.

Table 2
WIRC+Pol Asteroid Results

Asteroid	Date	Midpoint UT	Phase Angle (deg)	Filter	Polarization P_r [a]	Polarization Angle θ_r [b] (deg)
S-Complex						
3 Juno	2021-05-30	07:53	6.0	*J*	-0.74 ± 0.02	80.5 ± 0.5
3 Juno	2021-05-30	07:53	6.0	*H*	-0.88 ± 0.01	82.0 ± 0.5
3 Juno	2021-06-26	07:18	8.6	*J*	-0.89 ± 0.01	85.2 ± 0.9
3 Juno	2021-06-26	07:18	8.6	*H*	-0.85 ± 0.01	62.1 ± 0.6
3 Juno	2021-09-04	03:56	18.4	*J*	-0.46 ± 0.04	77.8 ± 0.9
3 Juno	2021-09-04	03:56	18.4	*H*	-0.43 ± 0.04	85.0 ± 0.5
7 Iris	2021-09-04	11:45	30.0	*J*	0.81 ± 0.03	172.7 ± 0.4
7 Iris	2021-09-04	11:45	30.0	*H*	0.67 ± 0.02	173.6 ± 0.2
7 Iris	2021-11-08	12:32	29.0	*J*	0.74 ± 0.04	6 ± 1
7 Iris	2021-11-08	12:32	29.0	*H*	0.61 ± 0.02	16.9 ± 0.1
15 Eunomia	2019-08-30	07:50	9.5	*J*	-0.99 ± 0.02	84.2 ± 0.2
15 Eunomia	2021-02-03	05:47	5.6	*J*	-0.89 ± 0.01	84.2 ± 0.1
15 Eunomia	2021-02-03	05:47	5.6	*H*	-0.82 ± 0.01	89.5 ± 0.1
20 Massalia	2021-11-08	12:01	28.7	*J*	0.74 ± 0.04	169.0 ± 0.5
20 Massalia	2021-11-08	12:01	28.7	*H*	0.81 ± 0.02	170.2 ± 0.2
C-Complex						
1 Ceres	2021-09-04	10:57	21.0	*J*	0.84 ± 0.02	157.7 ± 0.5
1 Ceres	2021-09-04	10:57	21.0	*H*	0.88 ± 0.02	163.8 ± 0.2
1 Ceres	2021-11-08	10:39	8.3	*J*	-1.74 ± 0.02	83.4 ± 0.1
1 Ceres	2021-11-08	10:39	8.3	*H*	-1.61 ± 0.03	86.6 ± 0.1
2 Pallas	2019-03-17	09:35	13.9	*J*	-0.97 ± 0.01	87.4 ± 0.2
2 Pallas	2019-03-17	10:10	13.9	*H*	-0.83 ± 0.01	90.3 ± 0.2
2 Pallas	2021-05-30	11:19	17.5	*J*	-0.29 ± 0.01	79 ± 2
2 Pallas	2021-05-30	11:19	17.5	*H*	-0.24 ± 0.02	109.1 ± 0.5
2 Pallas	2021-06-26	10:44	18.0	*J*	-0.15 ± 0.03	100.4 ± 6
2 Pallas	2021-06-26	10:44	18.0	*H*	-0.34 ± 0.01	115.3 ± 0.1
2 Pallas	2021-09-04	07:32	3.2	*J*	-1.29 ± 0.02	83.0 ± 0.6
2 Pallas	2021-09-04	07:32	3.2	*H*	-1.22 ± 0.01	83.2 ± 0.4
2 Pallas	2021-11-08	04:21	17.4	*J*	-0.27 ± 0.01	92 ± 6
2 Pallas	2021-11-08	04:21	17.4	*H*	-0.10 ± 0.02	78 ± 3
145 Adeona	2021-11-08	07:02	6.7	*J*	-1.63 ± 0.03	84.2 ± 0.2
145 Adeona	2021-11-08	07:02	6.7	*H*	-1.69 ± 0.03	85.3 ± 0.2

Notes.
[a] Polarization measurement P_r has been rotated such that positive values represent polarization perpendicular to the Sun–asteroid–telescope scattering plane and negative values represent polarization in the scattering plane.
[b] The angle of the polarization vector, rotated such that 0° is aligned perpendicular to the scattering plane.

and λ is the wavelength of observation. For our *J*- and *H*-band measurements, this results in a depolarization of the standard value of 0.461 for *J* and 0.250 for *H*. The Serkowski et al. (1975) correction was determined using the *U*, *B*, *V*, and *R* bandpasses only, so there is an unknown uncertainty associated with extending this to *J* and *H*. The angle of polarization (θ) in the near-infrared was assumed to be the same as for the literature measurements.

Our measurements of unpolarized standards generally show absolute polarization values that scatter around the expected 0.1% level. However, some standards (e.g., HD 35076 and HD 203843) repeatedly show measured polarizations larger than this on different nights. This could be due to instrumental polarization. A more likely explanation is that these sources are unpolarized at visible wavelengths but have nonzero polarization in the near-infrared, given their measured repeatability and the nondetection of polarization for other stars. We assess the instrumental polarization by looking at the measurement scatter for unpolarized standards observed multiple times (either within a run or between runs). We show in Figure 1 a histogram of the maximum change in polarization between observations for multiply measured unpolarized standards. The mean of these values is around 0.1%, consistent with the accuracy expected from previous calibration analyses (Tinyanont et al. 2019a; Millar-Blanchaer et al. 2021).

Observations of polarized standards allow us to check for potential instrumental depolarization and validate the measured polarization angle. We show in Figure 2 the results of our comparison of our measured values to literature values. It is important to note that because these literature values are scaled via a depolarization factor to correct for wavelength-dependent polarization, the true uncertainty on these measurements is certainly larger than the quoted values that are adopted from the visible measurements and may contain systematic errors as well. This could be potentially problematic, as it would be

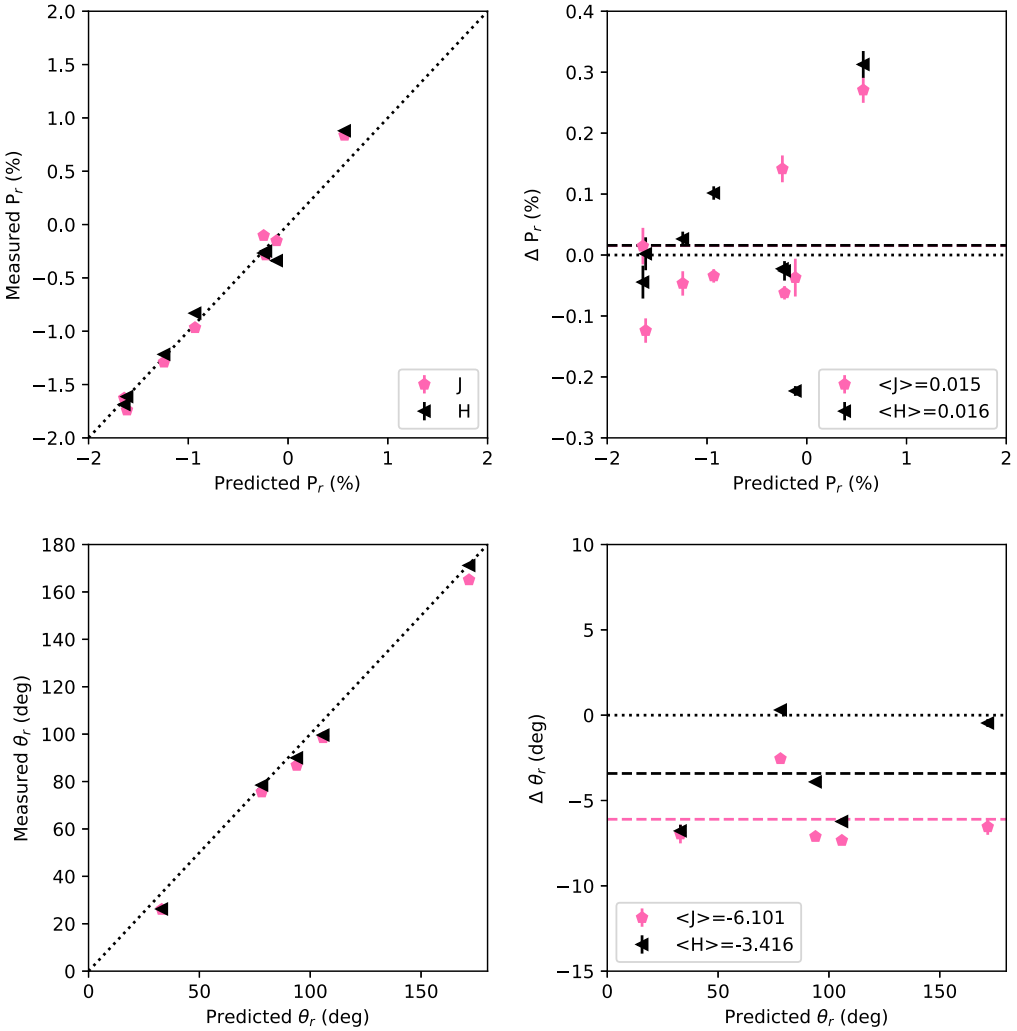

Figure 3. Comparison of predicted and measured polarization degrees and angles for C-complex asteroids, which are not expected to show any chromatic variations. Plot layout is the same as shown in Figure 2. Polarization degree P here is given in the typical fashion for asteroid measurements, where negative values indicate polarization in the scattering plane and positive values polarization perpendicular to it, and no wavelength-dependent scaling has been applied. Polarization angles were only compared for cases where the predicted polarization was $|P| > 0.25\%$.

difficult to distinguish instrumental depolarization from an incorrect scaling assumption.

The angle of polarization would not be expected to be changed by depolarization due to diminishing dust absorption. However, if the intervening dust was causing a rotation in the polarization angle, this effect would likely show a wavelength dependence. A potential example of this is the standard HD 17747, which has a literature angle of polarization at V band of $139\overset{\circ}{.}7$ but measured angles of polarization at J and H bands of 125° and 113°, respectively.

Due to these effects, visible-light polarimetric standards are imperfect for the analysis we hope to perform, but they do provide some level of validation of the system and instrument. From our investigation of polarized standard stars, and with the caveats above, we can see that WIRC+Pol reproduces predicted degrees of polarization to within 0.1% as expected, though the angle of polarization appears to show an offset of $\Delta\theta \sim -10°$, with a scatter larger than the statistical uncertainties. These results are consistent with the polarization accuracy and $\Delta\theta = -15°$ offset found in Millar-Blanchaer et al. (2021).

4. Results

We present in Table 2 our measurements of asteroids in the S taxonomic complex (S, S/K, and Sk/Sq taxonomic types from Neese 2017) and C taxonomic complex (C, B, and Ch taxonomic types from Neese 2017). Here we present the degree P_r and angle θ_r of the measure polarization after rotation into the scattering plane. P_r is listed as a positive value if it is perpendicular to the scattering plane at the time of observation and negative if it is parallel to the plane, in the typical convention for asteroid polarimetry. The θ_r angles have not been corrected for the offset discussed above, and after such correction they are consistent with purely parallel or perpendicular scattering for larger polarization values.

Uncertainties on the broadband measurements include only the statistical uncertainties of the measurements; systematic and instrumental polarization uncertainties are ∼0.1% as described above. We expect that there are correlated errors between wavelength channels, and as such the broadband uncertainties presented here may underestimate the true uncertainty somewhat. As our survey progresses, the scatter on repeated measurements of the same objects will allow us to set empirical constraints on the errors.

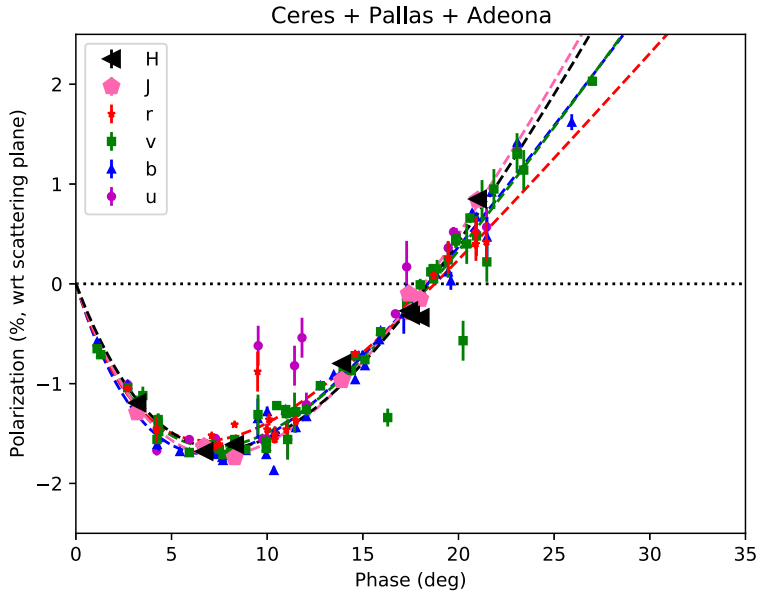

Figure 4. Polarimetric phase curve for three C-complex asteroids: Ceres, Pallas, and Adeona. *J*- and *H*-band data are presented in this manuscript, while *u*-, *b*-, *v*-, and *r*-band data for these three objects are from the Asteroid Polarimetric Database (Lupishko 2022). Functional form fits to the data using Equation (1) are shown with dashed lines, with the color of the line corresponding to the bandpass being fit.

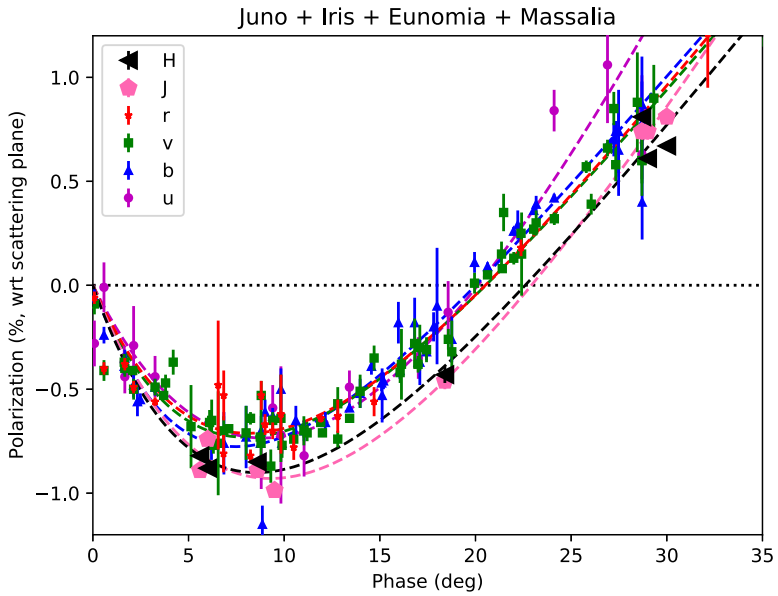

Figure 5. Polarimetric phase curve for four S-complex asteroids: Juno, Iris, Eunomia, and Massalia. *J*- and *H*-band data are presented in this manuscript, while *u*-, *b*-, *v*-, and *r*-band data for these three objects are from the Asteroid Polarimetric Database (Lupishko 2022). Functional form fits to the data using Equation (1) are shown with dashed lines, with the color of the line corresponding to the bandpass being fit.

In the course of our asteroid investigations it became clear that the C-complex asteroids observed do not show any wavelength dependence on their expected polarization. Further, the angle of polarization on the sky is fixed by the observing geometry and also will not have a wavelength dependence. As such, we can use bright C-complex asteroids as standards to validate the measured polarization degree and angle of WIRC +Pol. Using asteroids as a standard has an added layer of complexity, as the expected polarization degree and on-sky angle for these objects will be time dependent as the viewing geometry changes. They also cannot always be used as polarized standards, as near the inversion angle they will be expected to be unpolarized. These caveats aside, the lack of wavelength dependence on both polarization degree and angle outweighs the added planning difficulty.

We show in Figure 3 a comparison of our measured *J* and *H* polarization degrees and angles for C-type asteroids compared to the values predicted based on visible-light polarimetric behavior (with no chromatic correction) and the scattering geometry at the time of observation. Angle of polarization θ_r

Table 3
Asteroid Polarization Phase Curve Fits

Band	A	k	d	$P_{\rm min}$ (%)	$\alpha_{\rm min}$ (deg)	h	α_0 (deg)
S-Complex							
u	6^{+5}_{-2}	$0.21^{+0.1}_{-0.05}$	14^{+9}_{-4}	$-0.75^{+0.08}_{-0.06}$	$8.8^{+0.7}_{-0.7}$	$0.116^{+0.007}_{-0.007}$	$20.1^{+0.7}_{-0.5}$
b	$2.2^{+0.2}_{-0.2}$	$0.108^{+0.007}_{-0.007}$	$6.2^{+0.7}_{-0.6}$	$-0.78^{+0.02}_{-0.02}$	$7.5^{+0.3}_{-0.3}$	$0.094^{+0.003}_{-0.004}$	$20.0^{+0.2}_{-0.2}$
v	$2.4^{+0.2}_{-0.2}$	$0.109^{+0.009}_{-0.006}$	$7.1^{+0.7}_{-0.6}$	$-0.73^{+0.02}_{-0.01}$	$7.9^{+0.2}_{-0.2}$	$0.091^{+0.02}_{-0.03}$	$20.6^{+0.1}_{-0.2}$
r	$2.5^{+1.5}_{-0.7}$	$0.12^{+0.05}_{-0.03}$	8^{+4}_{-2}	$-0.71^{+0.03}_{-0.04}$	$8.1^{+0.9}_{-0.7}$	$0.09^{+0.01}_{-0.01}$	$20.8^{+0.8}_{-0.7}$
J	$3.8^{+0.4}_{-0.5}$	$0.15^{+0.01}_{-0.01}$	10^{+1}_{-1}	$-0.93^{+0.01}_{-0.01}$	$9.4^{+0.2}_{-0.3}$	$0.112^{+0.003}_{-0.004}$	$23.0^{+0.2}_{-0.3}$
H	$2.7^{+0.3}_{-0.2}$	$0.113^{+0.009}_{-0.006}$	$7.1^{+0.9}_{-0.5}$	$-0.90^{+0.1}_{-0.1}$	$8.5^{+0.3}_{-0.3}$	$0.098^{+0.004}_{-0.003}$	$22.6^{+0.3}_{-0.3}$
C-Complex							
b	$4.9^{+0.2}_{-0.1}$	$0.26^{+0.01}_{-0.01}$	$5.6^{+0.3}_{-0.2}$	$-1.71^{+0.01}_{-0.01}$	$6.88^{+0.1}_{-0.07}$	$0.225^{+0.004}_{-0.003}$	$18.4^{+0.1}_{-0.1}$
v	$5.4^{+0.3}_{-0.2}$	$0.28^{+0.01}_{-0.01}$	$6.6^{+0.3}_{-0.3}$	$-1.63^{+0.01}_{-0.02}$	$7.22^{+0.09}_{-0.09}$	$0.226^{+0.005}_{-0.005}$	$18.6^{+0.1}_{-0.1}$
r	$4.1^{+0.4}_{-0.4}$	$0.22^{+0.02}_{-0.02}$	$5.1^{+0.5}_{-0.5}$	$-1.58^{+0.03}_{-0.02}$	$6.7^{+0.2}_{-0.2}$	$0.19^{+0.01}_{-0.01}$	$18.7^{+0.3}_{-0.2}$
J	$7.5^{+0.4}_{-0.4}$	$0.37^{+0.02}_{-0.01}$	$8.3^{+0.5}_{-0.4}$	$-1.72^{+0.01}_{-0.02}$	$7.50^{+0.07}_{-0.08}$	$0.265^{+0.005}_{-0.003}$	$18.2^{+0.04}_{-0.04}$
H	$7.8^{+0.5}_{-0.5}$	$0.37^{+0.02}_{-0.02}$	$9.0^{+0.5}_{-0.5}$	$-1.65^{+0.02}_{-0.02}$	$7.67^{+0.07}_{-0.06}$	$0.257^{+0.004}_{-0.005}$	$18.4^{+0.02}_{-0.02}$

was only compared for observing dates where the predicted polarization degree was expected to be greater than $|P_r| > 0.25$ to ensure that the angle measurements were significant. While the number of observations is currently limited, our initial results indicate that any systematic instrumental polarization is well below the 0.1% level, that the measurement scatter is consistent with the 0.1% expected value, and that there is an offset of $\Delta\theta \sim -5°$. This offset is somewhat lower than the θ offset seen for the polarized stars in this work or the offset calculated by Millar-Blanchaer et al. (2021). Future observations of C-type asteroids will refine this measurement.

5. Polarimetric Phase Curves

To search for changes in polarization behavior with wavelength, we combined our measurements obtained in the near-infrared J and H bands with literature measurements of shorter-wavelength polarization data that are found in the Asteroid Polarimetric Database (Lupishko 2022). For this initial investigation we combined data from multiple different asteroids of the same taxonomic complex to allow us to search for broader trends; future observations will seek to obtain full phase curves for individual objects, allowing for object-by-object comparisons as well.

We show our results for the C-complex asteroids in Figure 4 and for the S-complex asteroids in Figure 5. The change in polarization as a function of asteroid phase can be described by the equation from Muinonen et al. (2009):

$$P = A\,(e^{-\alpha/d} - 1) + k\alpha, \quad (1)$$

where A is an amplitude parameter, k is a slope parameter, and d is the width of the negative branch. By fitting this function to the polarimetric measurements, we can derive the phase curve parameters $P_{\rm min}$, $\alpha_{\rm min}$, h, and α_0 that are related to asteroid physical properties. The fitted parameters and derived phase curve parameters for the S- and C-complex objects are given in Table 3, along with the 16th and 84th percentile uncertainty ranges.

We find that the C-complex objects do not show any significant change in their best-fit polarimetric phase curve at the phase angles investigated here from B band to H band, a wavelength span of over 1 μm. This is somewhat different than what was found by Belskaya et al. (2009), who find an expected change of +0.5% at $\alpha = 20°$, though it is consistent with their results for Ceres alone, which showed nearly no change over their bandpasses. This may indicate that object size is important for dictating wavelength dependence. This will be investigated further as we continue our survey of asteroid near-infrared polarimetric properties.

Conversely to what we see for the C-complex, for the S-complex objects we find that the phase curve appears to be offset or stretched to higher phase angles at longer wavelengths. This is comparable to what was observed by Belskaya et al. (2009) in direction and magnitude, though we find a change between r and J bands while they found a change from U to i. From the results shown in Masiero et al. (2009), this behavior is what would be expected for a change in the index of refraction n of the surface material. The interplay between the changing wavelength of light and the size distribution of scattering elements could also be a contributing factor in the observed differences. Using the relationship described by Gil-Hutton & García-Migani (2017),

$$n = (0.0403 \pm 0.008\,2)\alpha_0 + (0.9438 \pm 0.165\,0),$$

we can infer that the magnitude of the expected index of refraction change would be $\Delta n \sim 0.09$ from R band to J band if the observed shift was due entirely to changing n.

Interestingly, the h slope values and $P_{\rm min}$ are comparable across all bands. If the fitted constants in the slope–albedo relationship (e.g., Cellino et al. 2015) are not wavelength dependent, then this would imply that the geometric albedos are the same across wavelengths. These findings are preliminary, though, and full phase curve coverage for individual objects will help untangle any effects due to differences in surface composition between objects within the S-complex.

6. Conclusions

We have presented initial results of our survey of asteroid polarimetric properties in the near-infrared using the WIRC +Pol instrument on the Palomar 200-inch telescope. Our measurements of standard stars confirm that the instrument is capable of providing absolute polarimetric sensitivity at the 0.1% level in both J and H bands. Polarization of starlight by intervening dust is strongly wavelength dependent,

complicating this verification, but our observations of the polarization of C-complex asteroids indicate that these objects have reliable polarization degrees and angles from visible to near-infrared wavelengths and could be used for verification of the calibration of near-infrared polarimeters. Further polarimetric observations of C-complex asteroids in the near-infrared are encouraged to ensure that there are no systematic issues arising from use of these objects as calibration targets.

We also presented phase curves for seven S-complex and C-complex asteroids. C-complex asteroids show no significant changes in their polarization phase curves as a function of wavelength. In contrast, S-complex objects do show a significant change, most notable as an increase in polarimetric inversion angle. This may be linked to a change in the index of refraction of the surface material as a function of wavelength.

Our initial findings demonstrate the need for a more complete survey of the near-infrared polarimetric properties of different asteroid taxonomies. A specific focus on obtaining full phase curve coverage for individual objects will help disentangle changes among objects within a spectral class from differences between classes. Future WIRC+Pol observations will allow us to build a more complete picture of the physical properties and mineral makeup of the small bodies of our solar system.

The authors would like to thank the Palomar staff for their dedicated support and assistance that enabled our WIRC+Pol observing runs, especially as the COVID-19 pandemic upended regular operating procedures. We also thank the referees for their comments and suggestions that improved this paper. Based on observations obtained at the Hale Telescope, Palomar Observatory, as part of a continuing collaboration between the California Institute of Technology, NASA/JPL, Yale University, and the National Astronomical Observatories of China. This research made use of Photutils, an Astropy package for detection and photometry of astronomical sources (Bradley et al. 2019).

ORCID iDs

Joseph R. Masiero https://orcid.org/0000-0003-2638-720X

References

Belskaya, I. N., Levasseur-Regourd, A.-C., Cellino, A., et al. 2009, Icar, 199, 97
Bradley, L., Sipőcz, B., Robitaille, T., et al. 2019, astropy/photutils: v0.7.2, Zenodo, doi:10.5281/zenodo.3568287
Cañada-Assandri, M., Gil-Hutton, R., & Benavidez, P. 2012, A&A, 542, A11
Cellino, A., Bagnulo, S., Gil-Hutton, R., et al. 2015, MNRAS, 451, 3473
Cellino, A., Gil Hutton, R., di Martino, M., et al. 2005, Icar, 179, 304
Gil-Hutton, R., & Cañada-Assandri, M. 2011, A&A, 529, A86
Gil-Hutton, R., & Cañada-Assandri, M. 2012, A&A, 539, A115
Gil-Hutton, R., & García-Migani, E. 2017, A&A, 607, A103
Heiles, C. 2000, AJ, 119, 923
Hopfield, J. J. 1966, Sci, 151, 1380
Jones, T. ,. J., Stark, D., Woodward, C., et al. 2008, AJ, 135, 1318
Kwon, Y., Ishiguro, M., Kwon, J., et al. 2019, A&A, 629, 121
Lupishko, D. 2022, Asteroid Polarimetric Database V2.0. urn:nasa:pds:asteroid_polarimetric_database::2.0. NASA Planetary Data System, doi:10.26033/hyf9-4762
Lyot, B. 1929, Ann. Obs. Meudon, 8, 1
Masiero, J., Hartzell, C., & Scheeres, D. 2009, AJ, 138, 1557
Millar-Blanchaer, M., Tinyanont, S., Jovanovic, N., et al. 2021, Proc. SPIE, 11447, 114475Y
Muinonen, K., Penttilä, A., Cellino, A., et al. 2009, M&PS, 44, 1937
Muinonen, K., Piironen, J., Shkuratov, Y., Ovcharenko, A., & Clark, B. 2002, in Asteroids III, ed. W. F. Bottke, Jr. et al. (Tucson, AZ: Univ. Arizona Press), 123
Neese, C. 2017, Asteroid Taxonomy V1.0. urn:nasa:pds:ast_taxonomy::1.0. NASA Planetary Data System, doi:10.26033/e1p3-xm59
Oishi, M., Kawara, K., Kobayashi, Y., et al. 1978, PASJ, 30, 149
Pan, K.-S., & Ip, W.-H. 2022, PSS, 212, 105412
Serkowski, K., Mathewson, D. S., & Ford, V. L. 1975, ApJ, 196, 261
Shkuratov, Y., Muinonen, K., Bowell, E., et al. 1994, EM&P, 65, 201
Tinyanont, S., Millar-Blanchaer, M. A., Jovanovic, N., et al. 2019a, Proc. SPIE, 11132, 1113209
Tinyanont, S., Millar-Blanchaer, M. A., Nilsson, R., et al. 2019b, PASP, 131, 025001
Wilson, J. C., Eikenberry, S. S., Henderson, C. P., et al. 2003, Proc. SPIE, 4841, 451
Zellner, B., Gehrels, T., & Gradie, J. 1974, AJ, 79, 1100
Zellner, B., & Gradie, J. 1976, AJ, 81, 262